nature geoscience

Article

https://doi.org/10.1038/s41561-025-01726-z

North Pacific ocean–atmosphere responses to Holocene and future warming drive Southwest US drought

Received: 1 October 2024

Accepted: 21 May 2025

Published online: 9 July 2025

Check for updates

Victoria L. Todd[1] ✉, Timothy M. Shanahan[1], Pedro N. DiNezio[2], Jeremy M. Klavans[2], Peter J. Fawcett[3], R. Scott Anderson[4], Gonzalo Jiménez-Moreno[5], Allegra N. LeGrande[6,7], Francesco S. R. Pausata[8], Alexander J. Thompson[9] & Jiang Zhu[10]

The Southwest United States is experiencing severe and persistent drought, although uncertainties regarding the causes limit our ability to predict changes in water availability. The severity of the current drought has been attributed to a combination of warming and natural changes in atmospheric circulation, suggesting that current rainfall deficits may improve as natural oscillations reverse sign. Here we use new leaf-wax stable isotope reconstructions and simulations for the mid-Holocene (6 thousand years ago) and demonstrate that moderate warming of the Northern Hemisphere can produce drought over the Southwest United States through an ocean–atmosphere response originating in the North Pacific. The patterns of ocean warming and rainfall change resemble the negative phase of the Pacific Decadal Oscillation, indicating that this mode can be excited by external forcings. A similar response to warming is evident in future projections, leading to sustained winter precipitation deficits through the mid-twenty-first century. However, the magnitudes of past and current precipitation deficits associated with this North Pacific response are systematically underestimated in models, possibly due to a weak coupling of ocean–atmosphere interactions. Projections may also underestimate the magnitude of this precipitation response to changes in the North Pacific, leading to greater drought risk in this already water-poor region.

Semiarid regions around the world have been experiencing persistent drought over the past few decades[1]. Among them, the Southwest United States is experiencing the worst megadrought in the past 1,200 years[2]. The leading explanation for persistent drought in this region is natural processes within the climate system, involving stochastic atmospheric variability, ocean dynamics and coupled tropical ocean–atmosphere interactions[3–5]. Anthropogenic warming can also drive drought via increased evaporative demand[6,7], but a human influence on precipitation changes has not been established, mainly because the response of atmospheric circulation patterns to warming patterns is uncertain[8]. The influence of global temperatures on precipitation declines in semiarid regions such as the Southwest United States cannot be studied using historical observations alone because observed trends could be explained by natural variability in the climate system[8–10]. This complicates the attribution of the observed drought, and hence its prediction. Furthermore, while the magnitude of the current drought appears to be exceeding the limits of simulated variability[8,9], the mechanisms driving externally forced drought in models remain unclear[10], hindering predictions.

A full list of affiliations appears at the end of the paper. ✉e-mail: victoriatodd@utexas.edu

https://doi.org/10.1038/s41561-025-01726-z

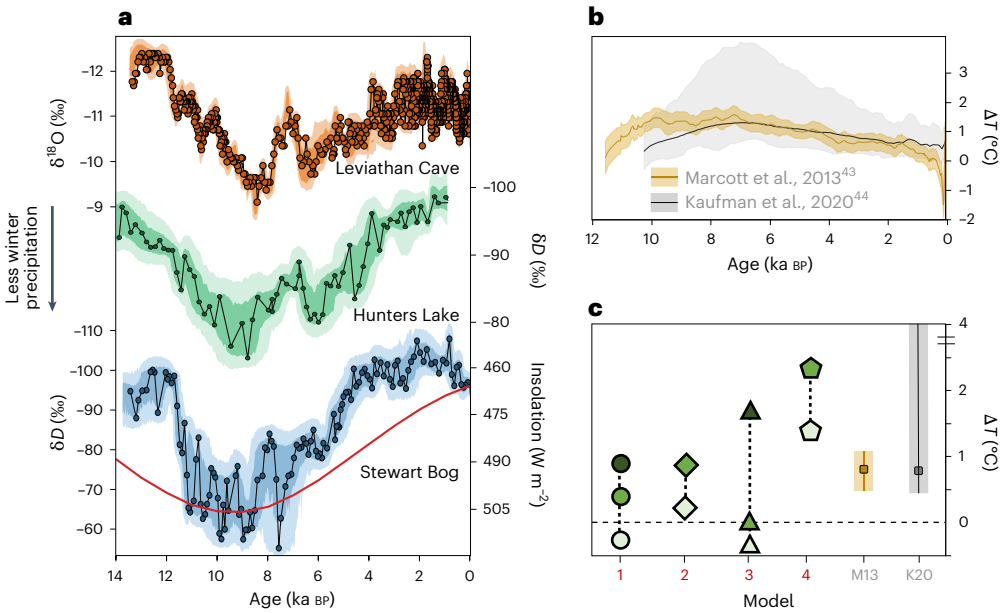

Fig. 1 | Proxy palaeoclimate changes in the Southwest United States. **a**, High-resolution stable isotope records reflecting moisture source changes over the past 14 kyr from Leviathan Cave, Nevada[14] (orange); Hunters Lake, Colorado (green) (this study); and Stewart Bog, New Mexico (blue) (this study), compared with July insolation at 65° N. **b**, Mean 30–90° N temperature syntheses (N = 73, gold shading = ±1σ; N = 1,319, grey shading = ±2σ; refs. 43,44). **c**, 6 ka 30–90° N temperature anomalies in CESM1.2 (1, circles), CCSM4-Toronto (2, diamonds), GISS-E2-G (3, triangles) and EC-Earth (4, pentagons) without vegetation change (light green), with prescribed 'Green Sahara' (green), and with both high- and low-latitude prescribed vegetation (dark green), compared with mean temperatures from M13 (ref. 43) (gold, shading = ±1σ) and K20 (ref. 44) (grey, shading = ±2σ) reconstructions. Black dotted lines emphasize the prescribed vegetation simulations conducted with the same model.

Palaeoclimate archives can provide insights into the causes of past and future droughts by allowing us to investigate how the climate system has responded in the past to external forcings[11]. For example, during the mid-Holocene (6 thousand years ago (ka)), the Southwest United States experienced widespread and prolonged aridity in response to changes in solar insolation[12–14]. Proxy data syntheses and theory indicate that mid-Holocene drying could have been driven by shifts in the position of the winter storm track directly forced by summer insolation-driven changes in high-latitude temperature and a weakening of the Equator-to-Pole temperature gradient[12–16]. However, models and proxy data disagree on the magnitudes and spatial patterns of Holocene precipitation changes over western North America[17]. These discrepancies may be partly due to the lack of quantitative proxy precipitation estimates; at many sites, the interpretation of precipitation proxies is complicated by changes in seasonality, with mid-Holocene reductions in winter precipitation accompanied by insolation-driven increases in the North American summer monsoon[15,18,19]. This makes our understanding of the magnitude, spatial extent and causes of drought in this water-dependent area of the United States less certain.

To study the mechanisms of forced drought in the Southwest United States, we combine new and existing palaeoclimate records with climate model simulations and proxy data syntheses for the mid-Holocene, a past interval with evidence of Northern Hemisphere warming[13,14]. Seasonal precipitation changes were quantified using two new leaf-wax isotope records (Stewart Bog (SB), New Mexico, and Hunters Lake (HL), Colorado; Extended Data Fig. 1) providing new constraints on mid-Holocene precipitation changes in the water-critical Rocky Mountains. In this region, the isotopic composition of precipitation is dominated by changes in the relative proportions of winter and summer moisture sources[14,20–22]. Winter precipitation tends to have stable isotope values that are significantly more negative (δD_{SB}: −116 ± 10‰; δD_{HL}: −153 ± 5‰) than summer monsoon precipitation[20,23] (δD_{SB}: −56 ± 8‰; δD_{HL}: −60 ± 5‰; Extended Data Fig. 2). To quantify changes in seasonal precipitation from the leaf-wax record, we developed a Bayesian isotope-mixing model (Methods). The model assumes that total precipitation was lower than today (mid-Holocene precipitation (MH_{precip}) ≤ preindustrial precipitation (PI_{precip})) on the basis of existing proxy data from across the Southwest United States[12–14] and uses the seasonal distributions of modern precipitation isotopes to estimate the range of possible winter and summer precipitation contributions consistent with the leaf-wax isotope records (Extended Data Fig. 3).

We compiled a new ensemble of 23 climate simulations using 17 different Earth system models, forced by 6 ka solar insolation and greenhouse gas forcings from Phase 3 of the Paleoclimate Intercomparison Project (PMIP)[24] to understand the drivers and forcing mechanisms of mid-Holocene drought. In addition, we include ten simulations with palaeoecologically realistic mid-Holocene vegetation changes prescribed over northern Africa (Green Sahara) or northern Africa and Siberia based on palaeovegetation proxy reconstructions (Supplementary Table 1 and Methods). This expanded mid-Holocene ensemble allows us to explore the robustness of the response to expanded vegetation, which a recent study suggested may be a critical component of the mid-Holocene climate response to orbitally driven insolation changes[25]. To evaluate the large-scale ocean and atmosphere responses associated with mid-Holocene drought, we performed a quantitative comparison of simulated sea surface temperature (SST) and precipitation against a synthesis of existing regional proxy reconstructions (Supplementary Table 2 and Methods). Finally, we performed a complementary set of sensitivity experiments using the atmosphere and land components of the Community Earth System Model (CESM1) with prescribed SSTs derived from the fully coupled simulations to isolate the atmospheric responses driving simulated mid-Holocene precipitation deficits in the Southwest United States using prescribing regional temperature responses derived from the fully coupled simulations (Supplementary Table 3 and Methods).

Quantifying mid-Holocene precipitation changes

The new leaf-wax isotope records reveal large, coherent shifts in winter precipitation delivered to the southernmost Rockies during the late

https://doi.org/10.1038/s41561-025-01726-z

glacial and Holocene periods (Fig. 1a). Both leaf-wax reconstructions display a shift to more positive δD values at ~11.7 ka, reflecting the onset of early to mid-Holocene winter drought. Mid-Holocene drought continues until ~5.5 ka, albeit with a transient shift to more negative isotope values between ~8.5 and 6.5 ka. Near-modern conditions are reached by ~4 ka, suggesting a nonlinear response modulated by diminishing regional feedbacks (for example, vegetation, soil moisture, ocean–atmosphere circulation). The pattern and timing of the changes are remarkably consistent with the changes in a published speleothem isotope record from Leviathan Cave in southern Nevada[14] (Fig. 1a, orange), suggesting that they reflect a coherent, large-scale climate response spanning the Southwest United States.

The magnitude of the peak early Holocene positive isotopic anomaly ~9 ka (Fig. 1a) is also similar at Hunters Lake and Leviathan Cave ($\Delta\delta D_{Hunters}$ = ~20‰ and $\Delta\delta D_{Leviathan}$ = 24‰; converted from $\delta^{18}O$ using global meteoric water line[26] ($\delta D = 8\delta^{18}O + 10‰$)) but differs from Stewart Bog ($\Delta\delta D$ = 47‰), which is located to the southeast of these sites. Despite these differences, our Bayesian isotope-mixing model indicates that these changes can be explained by similar minimum estimates for winter precipitation declines (Stewart Bog: −20%; Hunters Lake: −17%; Fig. 2b,d). However, modelled estimates of seasonal precipitation changes also depend on changes in summer precipitation, and previous studies have argued that mid-Holocene changes in summer insolation may have increased the strength of the early to mid-Holocene North American summer monsoon[14,18,19,27]. In climate model simulations, the summer precipitation response to insolation forcing is highly inconsistent outside the monsoon core in central-northern Mexico[18] making it difficult to estimate how much of an influence summer monsoon changes might have had. If we assume that monsoon precipitation did not increase at these study sites, the magnitude of winter precipitation decrease required to explain the leaf-wax records is even larger (SB: >33%; HL: >24%), supporting our inference that the mid-Holocene winter precipitation changes were large, regardless of changes in summer monsoon contributions. For the remainder of this paper, we use the minimum possible reduction in winter precipitation signal (for example, −17 to −20%; −41 to −43 mm yr^{-1} (ref. 28)) as a conservative estimate of these changes.

Warming drives winter precipitation changes

Standard PMIP3 (Fig. 2) and PMIP4[17] simulations with mid-Holocene forcings show small changes in winter precipitation over the Southwest United States (approximately −3.5%; Fig. 2). The inclusion of prescribed mid-Holocene vegetation results in much larger reductions (up to 12%), bringing the simulations closer to the palaeoclimatic evidence (Fig. 2a,c). Previous work has demonstrated that mid-Holocene vegetation changes can lead to hemispheric warming in models[25] that is consistent with temperature proxies. According to these studies, the vegetation-induced warming arises due to reduced land surface albedo and is propagated to the seasonal cycle through the reduction in sea ice and positive ice–albedo feedbacks (Supplementary Information and Extended Data Fig. 4). We find that this is a robust response in all of our mid-Holocene simulations with prescribed vegetation, with all models showing Northern Hemisphere warming. This warming is also accompanied by large reductions in winter precipitation over the Southwest United States, consistent with our proxy reconstructions, suggesting that this hemispheric warming drives these precipitation changes (Fig. 2a,c).

PDO-like state drives mid-Holocene precipitation changes

The simulations with prescribed vegetation show that mid-Holocene reductions in winter precipitation result from a coupled ocean–atmosphere response centred in the Pacific Ocean excited by hemispheric warming. This is evident in a distinct pattern of SST changes over the North Pacific, with intense surface warming extending across the mid- to high-latitude western Pacific surrounded by a 'horseshoe' pattern of

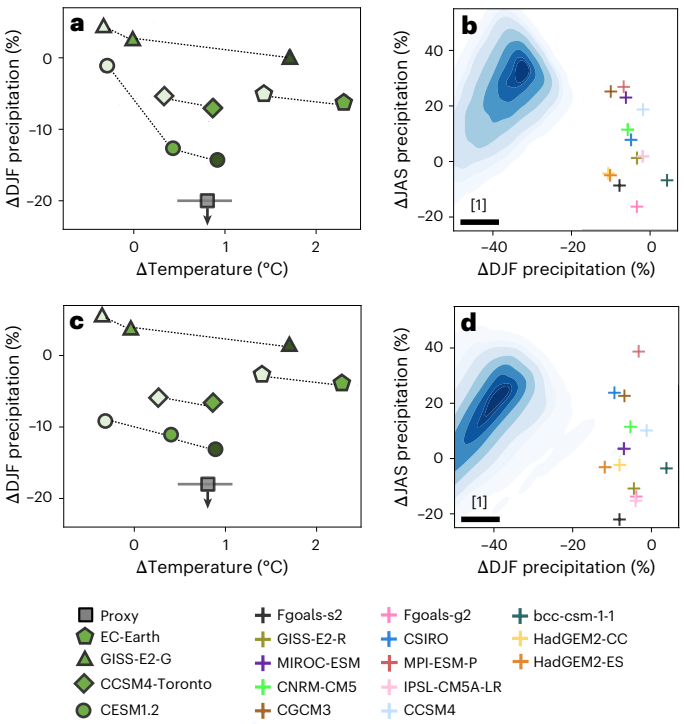

Fig. 2 | Model and proxy estimates of mid-Holocene (6 ka) winter precipitation anomalies. a,**c**, Simulated Northern Hemisphere (30–60° N) temperature and winter (December–January–February (DJF)) precipitation anomalies at Stewart Bog (**a**) and Hunters Lake (**c**) illustrate the systematic decrease in winter precipitation with hemispheric warming in models with prescribed preindustrial vegetation (light green), Green Sahara vegetation (green) and both high- and low-latitude vegetation (dark green); proxy estimates (grey squares) show median temperature ± 2σ from ref. 44 alongside the corresponding minimum winter precipitation anomaly (from **b** and **d**). Black dotted lines emphasize the prescribed vegetation simulations conducted with the same model. **b**,**d**, Comparison of PMIP3 model estimates of winter and summer (July–August–September (JAS)) precipitation changes at Stewart Bog (**b**) and Hunters Lake (**d**) with Bayesian isotope-mixing model estimates of mid-Holocene leaf-wax isotope values (blue shading). The range of estimates of mid-Holocene winter drying based on [1] (for the estimate of winter precipitation declines from the pollen synthesis of ref. 13) pollen data[13] is shown by black lines in **b** and **d** for comparison.

minimal surface warming or cooling to the east and a weak La Niña-like pattern in the tropical Pacific (Fig. 3b). This ocean temperature pattern is accompanied by a region of increased sea-level pressure over the North Pacific, indicating a weakened Aleutian Low. The North Pacific surface temperature and pressure patterns are reminiscent of the negative phase of the Pacific Decadal Oscillation (PDO; pattern correlation $r = 0.5197$, $P < 0.0001$ between the simulated SST response in Fig. 3b and historical PDO anomalies in Extended Data Fig. 5), which has been implicated in the length and severity of historical wintertime precipitation deficits over the Southwest United States[29–32]. However, unlike the observed PDO, which is a decadal-scale mode of variability presumed to be internally generated[3,6], in the mid-Holocene this pattern emerges as a sustained state in the North Pacific that dominates the climate over several millennia. Simulations without vegetation-driven hemispheric warming do not show this PDO-like pattern and instead cool over most of the North Pacific with a muted atmospheric response (Fig. 3a)[16]. Together, these results suggest that this negative PDO-like pattern emerges as a forced response to hemispheric warming (Extended Data Fig. 6 and Supplementary Discussion).

Support for this simulated ocean and atmospheric response comes from our proxy syntheses of changes in SSTs and North American

https://doi.org/10.1038/s41561-025-01726-z

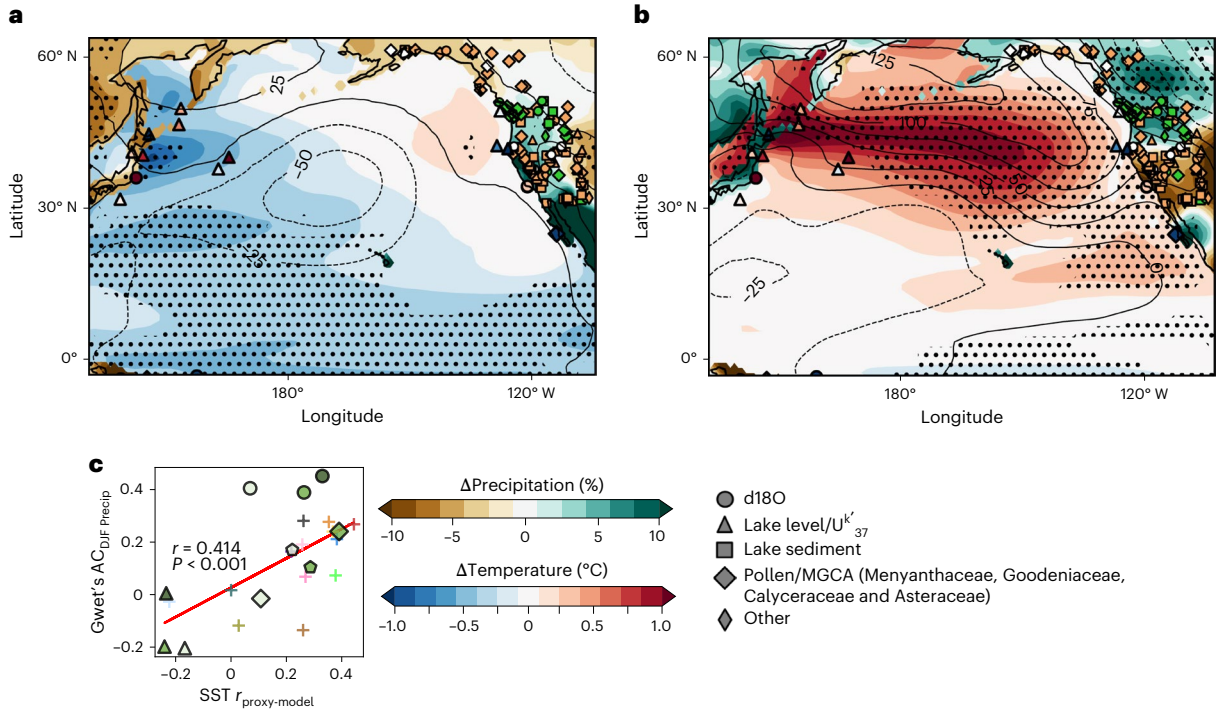

Fig. 3 | Proxy and model data comparison for the mid-Holocene. a,**b**, Ensemble mean winter (DJF) precipitation (shading), annual sea-level pressure (Pa) and surface temperature anomalies from preindustrial (shading) for models with preindustrial vegetation (**a**) and with prescribed 6 ka vegetation (**b**) and hemispheric warming. Stippling indicates where the majority of models in the ensemble agree ($n = 10$ out of 15 in **a** and $n = 6$ out of 8 in **b**). Symbols indicate proxy data sites used to assess agreement. **c**, The maximum winter (DJF) precipitation Gwet's AC value versus the annual SST pattern correlation value for all the models. Model symbols as in Fig. 2.

hydroclimate during the mid-Holocene (Supplementary Table 2). Although sparse, proxy SST data from the North Pacific show anomalies that are spatially consistent with the patterns of ocean temperature anomalies in the simulations with hemispheric warming (Fig. 3c). For example, marine proxy records show localized, enhanced warming (>2 °C) off the coast of Japan and cooling along the coast of California that are consistent with upwelling-induced SST patterns driven by a weakening of the Aleutian Low during the negative phase of the PDO.

Similarly, patterns of change in rainfall-sensitive proxies across western North America are in better agreement with simulated winter precipitation in simulations with prescribed vegetation and the PDO-like SST pattern (using the Gwet's AC and Cohen's Kappa metrics; Fig. 3, Extended Data Fig. 7, Supplementary Table 4 and Supplementary Discussion). Both proxies and winter precipitation anomalies display a tripole pattern, with widespread drying over the Southwest United States, wetter conditions over the Pacific Northwest and drying along the coast of Alaska (Fig. 3b), a pattern that is similar to the response seen in instrumental data during the negative phase of the PDO[33] when the Aleutian Low is also anomalously weak (Extended Data Fig. 5). Furthermore, the vegetation models with stronger proxy–model agreement in hydroclimate data are the ones that also show stronger SST correlations, supporting the direct link between North Pacific SST changes and precipitation changes over western North America (Fig. 3c). In the simulations without prescribed vegetation, the Pacific Northwest gets wetter, but high-latitude drying is too extensive and winter precipitation does not decrease over the Southwest United States, leading to weaker model–data agreement (Fig. 3a). In the simulations with prescribed vegetation, discrepancies occur in a relatively small subset of the data (4.3%), mostly in southwestern Alaska, where models show wetter conditions extending over a much broader area northwards and eastwards into the continent than indicated by the proxy data. We hypothesize that these regional differences may reflect model biases; in observations, increases in precipitation are highly localized along the coast due to topographic barriers to inland moisture transport (Supplementary Discussion and Extended Data Fig. 4).

An alternative explanation for the precipitation changes over North America during the mid-Holocene is changes in the tropical Pacific. Existing simulations[34–36] and proxy data[37–39] support decreased El Niño/Southern Oscillation variability and a more La Niña-like mean state, which should weaken the Aleutian Low via a Rossby wave teleconnection, modifying precipitation over the Southwest United States. However, while both the PMIP simulations and those with prescribed vegetation (veg) show similar tropical Pacific responses (change in equatorial Pacific SST gradient $MH_{PIveg} = -0.23$ K, $MH_{veg} = -0.27$ K), only the simulations with prescribed vegetation and the PDO-like pattern of SST changes in the Pacific show drying over the Southwest United States that is consistent with the proxy reconstructions (Fig. 3a,b).

Our sensitivity experiments (Methods and Supplementary Discussion) provide additional confirmation that changes in the North Pacific are the primary driver of regional reductions in winter precipitation over the Southwest United States. In the experiments forced with prescribed tropical Pacific SSTs derived from the fully coupled vegetation simulations, an atmospheric teleconnection typical of La Niña events is excited by the SST anomalies, weakening the Aleutian Low and shifting the storm tracks northwards. However, reductions in precipitation are restricted to westernmost North America along the Pacific coast (Extended Data Fig. 9). By contrast, prescribed changes in North Pacific SSTs drive an atmospheric teleconnection that emanates from the Kuroshio–Oyashio Extension, the region of pronounced warming in the North Pacific, producing an eastward shift in the Aleutian Low, which manifests as a lobe of anomalously high pressure along the west coast of North America. The development of this semi-permanent 'blocking high' deflects winter storms northwards, producing a band of reduced large-scale rainfall that spreads eastwards across the Southwest United States, consistent with the spatial extent of drought in proxy records (Extended Data Fig. 9).

https://doi.org/10.1038/s41561-025-01726-z

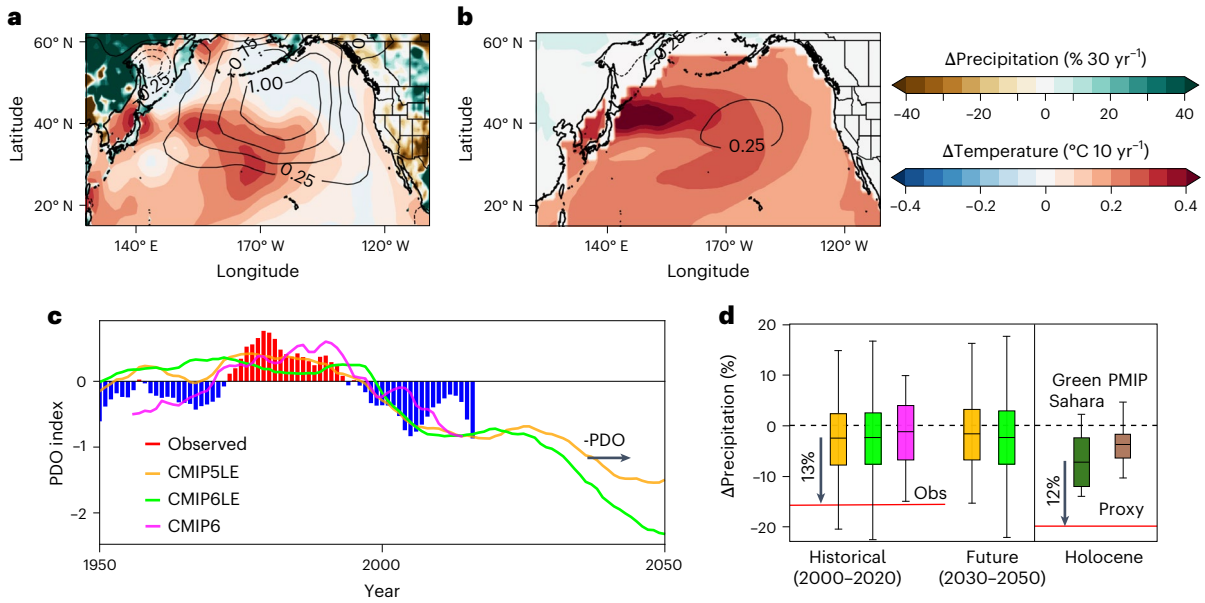

Fig. 4 | Emergence of a PDO pattern and Southwest US drought in observations and simulations. a,**b**, Winter (DJF) trends (1982–2019) in SST (shading), precipitation (shading) and sea-level pressure (contours, hPa 10 yr^{-1}) from observations[28,45,46] (**a**) and simulated by the combined CMIP5 and CMIP6 large ensembles (**b**; Supplementary Table 5). **c**,**d**, CMIP5LE (orange, $N = 270$), CMIP6LE (light green, $N = 165$) and CMIP6 historical (pink, $N = 337$) are shown in both panels. **c**, Normalized and 10-year running mean winter PDO index[47], compared with observations[46] (shading). **d**, Observed[28] (red line) and simulated Southwest US winter precipitation anomalies relative to 1977–1995 for the historical (2000–2020) and projected (2030–2050) periods (boxes represent 25th–75th percentiles, whiskers represent range and the line represents the median). Mid-Holocene winter precipitation anomalies relative to preindustrial from proxy estimate Stewart Bog (red line) and PMIP3 (brown, $N = 15$) and prescribed vegetation (dark green, $N = 8$) ensembles, shown for comparison. Southwest US area shown in Extended Data Fig. 1. Obs, observed.

Persistent PDO driven by greenhouse warming

It is conventionally accepted that the observed PDO arises naturally as a response to random atmospheric, oceanic and coupled tropical variability[3–5]. Our results for the mid-Holocene indicate that this paradigm needs to be reassessed and that persistent PDO states in the the North Pacific ocean–atmosphere system can be induced by external forcings associated with hemispheric warming. Anthropogenic greenhouse warming—with its stronger signature in the Northern Hemisphere due to polar and continental amplification—could drive an analogous response. We evaluated this possibility using large ensembles from CMIP5 (CMIP5LE, $n = 270$) and CMIP6 (CMIP6LE, $n = 165$), which allowed us to accurately isolate the forced responses[40,41] (J.M.K. et al., manuscript in preparation) in North Pacific SSTs, atmospheric circulation and drought (Methods and Supplementary Table 5). The CMIP5 and CMIP6 large ensembles show forced changes in SST and atmospheric circulation with a pattern characteristic of the negative phase of the PDO, suggesting a robust multimodel response to warming of the Northern Hemisphere. Furthermore, this forced PDO pattern persists well into 2050, driven by greenhouse warming and the abatement of aerosol emissions (Fig. 4c; J.M.K. et al., manuscript in preparation). This shift in the North Pacific ocean–atmosphere system has significant implications for the drought-sensitive Southwest United States[8,30,32].

Unexpectedly, while the CMIP ensembles all simulate a shift in the North Pacific to a negative phase of the PDO and a decline in winter precipitation, they underestimate the magnitude of precipitation changes to a negative PDO. In simulations of precipitation changes over the historical period (2000–2020), the precipitation response during a shift to the negative phase of the PDO is underestimated by 97.3% of the CMIP6LE simulations, by an average of 14% in the ensemble mean (−31.38 mm month^{-1} (ref. 28) from 1977 to 1995; Fig. 4d). This deficiency is rooted in two interrelated model errors. First, models underestimate the magnitude of the forced PDO pattern (J.M.K. et al., manuscript in preparation) that drives precipitation changes[6]. Second, the atmospheric model produces precipitation changes that are too small, even when forced with the observed PDO SST pattern[8] (Extended Data Fig. 10). In our Holocene model–proxy comparison, the atmospheric response to changes in the North Pacific SSTs is similarly weak (Fig. 3b), with winter precipitation underestimated by at least 12% (Figs. 2 and 4d). While a small percentage (2%) of the historical simulations produce precipitation deficits of similar magnitude to observations, suggesting that the severity of the current drought could be particularly unlucky[6,7], the similar deficiency in the Holocene model–data comparison presented here raises the question of whether models are underestimating the precipitation response to changes in the North Pacific ocean–atmosphere system. These model discrepancies could lead to much larger deficits in winter rainfall than predicted. Furthermore, our results suggest that these precipitation deficits will be maintained by a shift to a more permanent negative PDO-like state as long as hemispheric warming persists (see Supplementary Fig. 4 for longer-term projections, noting that these are based on divergent future forcings). Such sustained drying and intense reductions in winter precipitation would have catastrophic impacts across the Southwest United States, particularly in the Colorado River Basin, where scaling relationships point to reductions in flow that are at least twice as large as the change in precipitation[41,42].

Here we demonstrate that Northern Hemisphere warming can lead to the emergence of a coupled ocean–atmosphere response in the North Pacific resembling the negative phase of the PDO, resulting in widespread drought over the Southwest United States. During the mid-Holocene, warming induced by large-scale vegetation changes induced this response, leading to significant, regional-scale reductions in winter precipitation. Large ensembles of future warming simulations indicate that greenhouse warming leads to a similar response, causing a shift to a persistent negative PDO and a sustained drier climate state over the Southwest United States. However, the proxy–model mismatch in the magnitude of past precipitation responses to this negative PDO-like state also implies

that models may be underestimating the severity of future winter precipitation changes and the future risk of drought in the Southwest United States.

Online content

Any methods, additional references, Nature Portfolio reporting summaries, source data, extended data, supplementary information, acknowledgements, peer review information; details of author contributions and competing interests; and statements of data and code availability are available at https://doi.org/10.1038/s41561-025-01726-z.

References

1. Seneviratne, S. I. et al. in *Climate Change 2021: The Physical Science Basis* (eds Masson-Delmotte, V. et al.) Ch. 11 (Cambridge Univ. Press, 2021).
2. Williams, A. P., Cook, B. I. & Smerdon, J. E. Rapid intensification of the emerging southwestern North American megadrought in 2020-2021. *Nat. Clim. Change* **12**, 232–234 (2022).
3. Newman, M. et al. The Pacific decadal oscillation, revisited. *J. Clim.* **29**, 4399–4427 (2016).
4. Eyring, V. et al. in *Climate Change 2021: The Physical Science Basis* (eds Masson-Delmotte, V. et al.) Ch. 3 (Cambridge Univ. Press, 2021).
5. Hoesly, R. M. et al. Historical (1750–2014) anthropogenic emissions of reactive gases and aerosols from the Community Emissions Data System (CEDS). *Geosci. Model Dev.* **11**, 369–408 (2018).
6. Seager, R. et al. Ocean-forcing of cool season precipitation drives ongoing and future decadal drought in southwestern North America. *NPJ Clim. Atmos. Sci.* **6**, 141 (2023).
7. Seager, R. et al. Dynamical and thermodynamical causes of large-scale changes in the hydrological cycle over North America in response to global warming. *J. Clim.* **27**, 7921–7948 (2014).
8. Lehner, F., Deser, C., Simpson, I. R. & Terray, L. Attributing the US Southwest's recent shift into drier conditions. *Geophys. Res. Lett.* **45**, 6251–6261 (2018).
9. Kuo, Y. N., Kim, H. & Lehner, F. Anthropogenic aerosols contribute to the recent decline in precipitation over the US Southwest. *Geophys. Res. Lett.* **50**, e2023GL105389 (2023).
10. Cook, B. I. et al. Megadroughts in the Common Era and the Anthropocene. *Nat. Rev. Earth Environ.* **3**, 741–757 (2022).
11. Tierney, J. E. et al. Past climates inform our future. *Science* **370**, eaay3701 (2020).
12. Hermann, N. W., Oster, J. L. & Ibarra, D. E. Spatial patterns and driving mechanisms of mid-Holocene hydroclimate in western North America. *J. Quat. Sci.* **33**, 421–434 (2018).
13. Routson, C. C. et al. Mid-latitude net precipitation decreased with Arctic warming during the Holocene. *Nature* **568**, 83–87 (2019).
14. Lachniet, M. S., Asmerom, Y., Polyak, V. & Denniston, R. Great Basin paleoclimate and aridity linked to Arctic warming and tropical Pacific sea surface temperatures. *Paleoceanogr. Paleoclimatol.* **35**, e2019PA003785 (2020).
15. Metcalfe, S. E., Barron, J. A. & Davies, S. J. The Holocene history of the North American Monsoon: 'known knowns' and 'known unknowns' in understanding its spatial and temporal complexity. *Quat. Sci. Rev.* **120**, 1–27 (2015).
16. Park, H. S. et al. Mid-Holocene Northern Hemisphere warming driven by Arctic amplification. *Sci. Adv.* **5**, eaax8203 (2019).
17. de Wet, C. B., Ibarra, D. E., Belanger, B. K. & Oster, J. L. North American hydroclimate during past warms states: a proxy compilation-model comparison for the Last Interglacial and the mid-Holocene. *Paleoceanogr. Paleoclimatol.* **38**, e2022PA004528 (2023).
18. Routson, C. C., Erb, M. P. & McKay, N. P. High latitude modulation of the Holocene North American Monsoon. *Geophys. Res. Lett.* **49**, e2022GL099772 (2022).
19. Bhattacharya, T. An energetic perspective on the Holocene North American Monsoon. *Geophys. Res. Lett.* **49**, e2022GL100782 (2022).
20. Tolley, D. G., Frisbee, M. D. & Campbell. A. R. in *Geology of the Las Vegas Region* Vol. 66 (eds Lindline, J. et al.) 303–312 (New Mexico Geological Society, 2015).
21. Dansgaard, W. Stable isotopes in precipitation. *Tellus* **16**, 436–468 (1964).
22. Tulley-Cordova, C. L., Putman, A. L. & Bowen, G. J. Stable isotopes in precipitation and meteoric water: sourcing and tracing the North American Monsoon in Arizona, New Mexico, and Utah. *Water Resour. Res.* **57**, e2021WR030039 (2021).
23. Bowen, G. J. & Revenaugh, J. Interpolating the isotopic composition of modern meteoric precipitation. *Water Resour. Res.* **39**, 1299 (2003).
24. Braconnot, P. & Kageyama, M. Shortwave forcing and feedbacks in Last Glacial Maximum and Mid-Holocene PMIP3 simulations. *Phil. Trans. R. Soc. A* **373**, 20140424 (2015).
25. Thompson, A. J., Zhu, J., Poulsen, C. J., Tierney, J. E. & Skinner, C. B. Northern Hemisphere vegetation change drives a Holocene thermal maximum. *Sci. Adv.* **8**, eabj6535 (2022).
26. Craig, H. Isotopic variations in meteoric waters. *Science* **133**, 1702–1703 (1961).
27. Lachniet, M. S., Du, X. & Dee, S. G. Elevated Grand Canyon groundwater recharge during the warm early Holocene. *Nat. Geosci.* **16**, 915–921 (2023).
28. Schneider, U., Becker, A., Finger, P., Rustemeier, E. & Ziese, M. *GPCC Full Data Monthly Product Version 2020 at 1.0°: Monthly Land-Surface Precipitation from Rain-Gauges Built on GTS-Based and Historical Data* (Global Precipitation Climatology Centre (GPCC) at Deutscher Wetterdienst, 2020); http://gpcc.dwd.de/
29. Schubert, S. et al. A US CLIVAR project to assess and compare the responses of global climate models to drought-related SST forcing patterns: overview and results. *J. Clim.* **22**, 5251–5272 (2009).
30. Chylek, P., Dubey, M. K., Lesins, G., Li, J. N. & Hengartner, N. Imprint of the Atlantic multi-decadal oscillation and Pacific decadal oscillation on southwestern US climate: past, present, and future. *Clim. Dyn.* **43**, 119–129 (2014).
31. Zhao, C. et al. Temperature increase reduces global yields of major crops in four independent estimates. *Proc. Natl Acad. Sci. USA* **114**, 9326–9331 (2017).
32. Erb, M. P., Emile-Geay, J., Hakim, G. J., Steiger, N. & Steig, E. J. Atmospheric dynamics drive most interannual US droughts over the last millennium. *Sci. Adv.* **6**, eaay7268 (2020).
33. Deser, C., Phillips, A. S. & Hurrell, J. W. Pacific interdecadal climate variability: linkages between the tropics and the North Pacific during boreal winter since 1900. *J. Clim.* **17**, 3109–3124 (2004).
34. Clement, A. C., Seager, R. & Cane, M. A. Suppression of El Niño during the Mid-Holocene by changes in the Earth's orbit. *Paleoceanography* **15**, 731–737 (2000).
35. Karamperidou, C., Di Nezio, P. N., Timmermann, A., Jin, F. F. & Cobb, K. M. The response of ENSO flavors to mid-Holocene climate: implications for proxy interpretation. *Paleoceanography* **30**, 527–547 (2015).
36. Karamperidou, C. & DiNezio, P. N. Holocene hydroclimatic variability in the tropical Pacific explained by changing ENSO diversity. *Nat. Commun.* **13**, 7244 (2022).
37. Cobb, K. M. et al. Highly variable El Niño–Southern Oscillation throughout the Holocene. *Science* **339**, 67–70 (2013).

38. Emile-Geay, J. et al. Links between tropical Pacific seasonal, interannual and orbital variability during the Holocene. *Nat. Geosci.* **9**, 168–173 (2016).
39. Carré, M. et al. High-resolution marine data and transient simulations support orbital forcing of ENSO amplitude since the mid-Holocene. *Quat. Sci. Rev.* **268**, 107125 (2021).
40. Scaife, A. A. & Smith, D. A signal-to-noise paradox in climate science. *NPJ Clim. Atmos. Sci.* **1**, 28 (2018).
41. Xiao, M., Udall, B. & Lettenmaier, D. On the causes of declining Colorado River streamflows. *Water Resour. Res.* **54**, 6739–6756 (2018).
42. Vano, J. et al. Understanding uncertainties in future Colorado River streamflow. *Bull. Am. Meteorol. Soc.* **95**, 59–78 (2014).
43. Marcott, S. A., Shakun, J. D., Clark, P. U. & Mix, A. C. A reconstruction of regional and global temperature for the past 11,300 years. *Science* **339**, 1198–1201 (2013).
44. Kaufman, D. et al. Holocene global mean surface temperature, a multi-method reconstruction approach. *Sci. Data* **7**, 201 (2020).
45. Kalnay, E. et al. The NCEP/NCAR 40-year reanalysis project. *Bull. Am. Meteorol. Soc.* **77**, 437–470 (1996).
46. Huang, B. et al. *NOAA Extended Reconstructed Sea Surface Temperature (ERSST) V***5** (NOAA National Centers for Environmental Information, 2017).
47. Phillips, A. S., Deser, C., Fasullo, J., Schneider, D. P. & Simpson, I. R. *Assessing Climate Variability and Change in Model Large Ensembles: A User's Guide to the Climate Variability Diagnostics Package for Large Ensembles* (National Center for Atmospheric Research (NCAR), 2020).

[1]Jackson School of Geosciences, The University of Texas at Austin, Austin, TX, USA. [2]Department of Atmospheric and Oceanic Sciences, The University of Colorado, Boulder, CO, USA. [3]The Department of Earth and Planetary Sciences, The University of New Mexico, Albuquerque, NM, USA. [4]School of Earth and Sustainability, Northern Arizona University, Flagstaff, AZ, USA. [5]Departamento de Estratigrafía y Paleontología, Universidad de Granada, Granada, Spain. [6]Center for Climate Systems Research, Columbia University, New York, NY, USA. [7]NASA Goddard Institute for Space Studies, New York, NY, USA. [8]Centre ESCER and GEOTOP, Department of Earth and Atmospheric Sciences, University of Quebec in Montreal, Montreal, Quebec, Canada. [9]Cooperative Institute for Research In Environmental Sciences, The University of Colorado, Boulder, CO, USA. [10]Climate and Global Dynamics Laboratory, National Center for Atmospheric Research, Boulder, CO, USA. ✉e-mail: victoriatodd@utexas.edu

https://doi.org/10.1038/s41561-025-01726-z

Methods

Study sites and age modelling

Stewart Bog is located in the Sangre de Cristo mountains of Northern New Mexico (latitude 35.83° N, longitude 105.73° W, elevation 3,119 m; Extended Data Fig. 1). It was formed in a depression in the landscape created by glacial retreat ~14.7 ka (ref. 48). The composite Stewart Bog record is based on three sediment cores—B1-4, B1-5 and B1-6—obtained using a Livingston square-rod piston corer[48]. Access to the site to obtain these cores was granted by the Pecos District Forest Service[48]. The age model for this composite core is based on the radiocarbon dating[49] of bulk organic carbon ($n = 5$), charcoal ($n = 2$) and wood ($n = 4$). In this study, we updated the sediment age–depth model using the IntCal20 calibration curve and the Bayesian age modelling programme RBACON[50].

Hunters Lake is a subalpine lake in the Southern Rockies (latitude 37.36° N, longitude 106.50° W, elevation 3,516 m). A long sediment core was retrieved using a modified Livingston piston corer, and a short core capturing the surface sediments was obtained to provide an uninterrupted lake record extending to the present[51]. Access to the site to obtain these cores was granted by the US Forest Service[51]. Six radiocarbon dates were obtained from the long sediment core, and ^{137}C and ^{210}Pb dating techniques were used to generate an age model for the uppermost surface core to establish an age model[51]. The sediment age–depth model was updated for this study using the IntCal20 calibration curve and the Bayesian age modelling programme RBACON[50].

Sampling and sample preparation

The 1 cc samples were taken every 4 cm from the Stewart Bog and Hunters Lake cores[52]. At Hunters Lake, we were unable to sample the uppermost short core because insufficient material remained for analysis. Lipids were extracted from freeze-dried sediments using MARS 5 Xpress microwave solvent extraction system using dichloromethane: methanol (MeOH) (9/1, v/v). Lipid extraction was performed by ramping the temperature slowly to 100 °C and holding for 10 min with continuous stirring. After extraction, samples were filtered and dried over a $NaSO_4$ column and evaporated under N_2. Total lipid fractions were loaded onto aminopropyl columns for solid phase extraction using Rapid Trace SPE stations and separated with hexane, isopropanol in hexane, and 2% formic acid in dichloromethane to isolate the apolar GDGT (glycerol dialkyl glycerol tetraether) and fatty acid fractions, respectively. The fatty acid fractions were then methylated in an acidified methanol solution (12 h at 50 °C). The resultant fatty acid methyl esters (FAMEs) were purified again over silica gel using dichloromethane before quantification and analysis.

Stable isotope analysis of FAMEs

Before stable isotope analysis, the fatty acid fraction of all samples was analysed (as FAMES) by gas chromatography flame ionization detection to assess purity and determine the concentrations of the target compounds. Hydrogen isotope analysis was performed by gas chromatography–pyrolysis–isotope ratio mass spectrometry on a Thermo Finnigan Delta V Plus mass spectrometer. Hydrogen reference gas and an internal propane gas standard were calibrated against a known *n*-alkane standard (the 'B4' mix, A. Schimmelmann, Indiana University). An external FAME standard was analysed multiple times during each run, and multiple injections of the propane gas standard were run with each sample and used to correct for sample drift and offsets. Samples were run in duplicate or triplicate, and standard deviations between injections were ~2‰ versus VSMOW. A mass balance correction was applied to account for the added methyl group during methylation. The δD values of the methylation methanol were determined by methylating a phthalic acid standard of known isotopic composition. In this study, we focus on the isotopic composition of the long-chain fatty acids (C_{28}, C_{30}) because they are less likely to be produced by aquatic or microbial sources.

Inferring δD_{precip} from δD_{wax}

Previous syntheses of modern leaf-wax samples have shown that leaf-wax δD (δD_{wax}) can provide a reliable archive of the past isotopic composition of precipitation source water[53]. However, a few complicating factors relating δD_{wax} to δD_{precip} need to be considered when interpreting leaf-wax reconstructions. First, there is a strong biological fractionation associated with the process of leaf-wax synthesis (ε_{wax}), which has been shown to vary as a function of plant type and biosynthetic pathway[53]. In proxy records, sedimentary δD_{wax} values reflect the combined biosynthetic fractionation of all the plants in the catchment, potentially complicating the interpretation of leaf-wax records. To quantitatively estimate the impact of these changes in our records, we estimated the relative abundance of C_3 and C_4 plants in this record using existing pollen data[48,51]. Between 6 ka and the preindustrial, there may have been as large as a 10% change in the abundance of C_3 plants (arboreal trees)[48,51]. Previous studies have suggested that there may be as much as a 19‰ offset in the fractionation factors for plants with these two photosynthetic pathways ($\varepsilon_{wax\text{-}C3} = -113‰$; $\varepsilon_{wax\text{-}C4} = -132‰$) (ref. 53). Given the changes in community plant composition indicated by the pollen data, this would have resulted in a shift in the fractionation factor of ~3‰ at Stewart Bog between the preindustrial and mid-Holocene[48,51]. This difference is within the errors of the mixing model calculations and probably the uncertainties in the estimates of endmember fractionation factors, so we did not apply any correction to the δD_{wax} data in this study. Evaporative fractionation can also cause offsets between the δD_{wax} and δD_{precip} values due to isotopic enrichment of the source water at the locus of leaf-wax synthesis. While this effect can be large in arid regions, studies of modern plants across the Southwest United States indicate that the offset between δD_{wax} and δD_{precip} is indistinguishable within uncertainties throughout the hydrologic year[54]. Given the uncertainties associated with any correction for plant water evaporation, we did not make any adjustments for this effect in our analysis.

Bayesian isotope-mixing model

A Bayesian stable isotope-mixing model was developed to estimate the proportion of seasonal moisture sources contributing to the stable isotope composition of a sample. For the publicly available MixSIAR Bayesian stable mixing model[55] used in this study, the following basic equation applies:

$$Y_j = \sum_k p_k \mu_{jk}^s$$

where for each of the j tracers, the mixture tracer value, Y_j is equal to the sum of the k source tracer means μ_{jk}^s multiplied by their proportional contribution to the mixture (p_k). Mixing models assume that (1) the sources contributing to the mixture are known and quantified, (2) tracers are conserved through the mixing process, (3) source mixture and tracer values are fixed (known and invariant), (4) the p_k terms sum to unity and (5) source tracer values differ[55]. The isotopic compositions of the modern precipitation sources for the Stewart Bog[20] and the Hunters Lake[23] sites were obtained to implement the model (Extended Data Fig. 1).

In this study, a major assumption is that the dominant control on past changes in the isotopic composition of precipitation between the mid-Holocene and the preindustrial is changes in the proportions of winter and summer precipitation. This assumption is based on previous studies, which indicated significant changes in the strength of the mid-Holocene monsoon and the winter storm track[12,14,18]. For this reason, these palaeo isotopic values are represented as a two-endmember mix between the monsoon and winter precipitation. The 'raw' lists of stable isotope measurements from the winter and summer seasons were used as priors in the model to preserve the uncertainty in the estimates for the source means and variances. These winter and summer isotopic values were represented as uniform prior distributions:

$$p_1 \approx U(0,1) = p_1 \approx U(0,1)$$

$$\sum_{i=1}^{n=2} p_i = 1$$

$$p_2 = 1 - p_1$$

MixSIAR assumes multivariate normality and estimates the variance–covariance matrix associated with the tracers for each source. Naïve priors were used for winter and summer precipitation proportions to reduce bias. The model was evaluated at two different times: the mid-Holocene and the preindustrial. The raw lists of stable isotope measurements from the mid-Holocene (6 ± 0.2 ka) and the preindustrial (calendar years 1850 to 1950) were used to construct normal distributions for the isotopic values of the mixtures. Process and residual error with covariance were incorporated into the model. Posterior distributions of the proportion of summer to winter precipitation during the mid-Holocene and preindustrial were used to calculate the percentage change in winter and summer precipitation.

Seasonal preindustrial precipitation amount data were retrieved from the ERA5 reanalysis dataset[56]. First, the distribution of the proportions of summer to winter precipitation (Supplementary Fig. 2) during the preindustrial calculated from the proxy records and the distribution of preindustrial seasonal precipitation amounts (ERA5 reanalysis) were compared via bootstrapping to calculate the possible combinations of winter and summer precipitation that would satisfy the proxy calculated ratios. Next we assumed that the sum of winter and summer precipitation during the mid-Holocene was less than that during the preindustrial. Then, 10,000 times we solved the equation:

$$\mathrm{MH}_{\mathrm{winter}} + \mathrm{MH}_{\mathrm{summer}} \leq \mathrm{PI}_{\mathrm{total}}$$

Where $\mathrm{MH}_{\mathrm{summer}} = \mathrm{MH}_{\mathrm{ratio}} \times \mathrm{MH}_{\mathrm{winter}}$

$\mathrm{MH}_{\mathrm{total}}$ is a half-normal distribution centred around the $\mathrm{PI}_{\mathrm{total}}$ with the same standard deviation as the $\mathrm{PI}_{\mathrm{total}}$; the assumption of this parametric shape was derived from the climate models, which show a shift in the mean precipitation during the mid-Holocene with the same standard deviation as during the preindustrial. For each realization of preindustrial and mid-Holocene seasonal precipitation amounts, the percentage change in precipitation was calculated, leading to the simulated range in possible values.

Synthesis of proxy precipitation and SST records

To assess the proxy–model agreement, we generated new syntheses of proxy reconstructions of SST from the North Pacific and proxy hydroclimate records from western North America, drawing from existing compilations and the published literature (Supplementary Table 2). For the SST synthesis (n = 88 records), we used existing published reconstructions from the synthesis of ref. 44 and supplemented it with additional key records from the North Pacific. In addition, we assembled a new synthesis of proxy hydroclimate data from western North America from the published literature (n = 138 records[12,14,57]; Supplementary Table 2). Our precipitation synthesis relies on a variety of proxy indicators, including lake level and status, $\delta^{18}O$ values of speleothems and lake carbonates, pollen, and a variety of sedimentological indicators (Supplementary Fig. 1). For the pollen-inferred hydroclimate changes, we deviated from the interpretations used in previous syntheses and relied on the LegacyClimate 1.0 database of modern analogue technique-based pollen transfer functions[57]. Only those sites showing a statistically significant precipitation reconstruction (significance tests from LegacyClimate 1.0 database) were included ($P > 0.1$; n = 52/341). Because quantitative transfer functions are either unavailable or highly uncertain for most precipitation proxies, and because our primary focus was on reconstructing the large-scale patterns of precipitation change, we categorized the records as wetter, drier or unchanged (at 6 ka) relative to the late Holocene (0–1 ka) and used the Cohen's Kappa and Gwet's AC metrics[58–60] to assess proxy–model agreement (Methods).

We used mean values for the mid-Holocene (6,000 ± 500 yr BP) and preindustrial (200 to 500 yr BP) to compute anomalies. To classify the hydroclimatic and SST data from each site, a T test was used first to determine whether the changes were statistically significant, given the variability in the reconstructions. All sites were then classified as wetter, drier, warmer, cooler or unchanged relative to the preindustrial.

Climate model experiments

To understand how the climate system changes under mid-Holocene conditions in climate model simulations, we compiled 24 existing mid-Holocene (6 ka) simulations (Supplementary Table 1) performed with 17 general circulation models). Of these, 13 simulations were from the PMIP3 project, including two that included dynamic vegetation changes (HadGEM2-CC, HadGEM2-ES). We also included 11 additional simulations, which allowed us to assess the influence of changes in prescribed vegetation. In two cases (CESM1.2 and GISS-E2), models were run with preindustrial vegetation, prescribed vegetation over the Sahara (for example, Green Sahara runs), and prescribed vegetation over the Northern Hemisphere + Green Sahara. Mid-Holocene simulations were forced by prescribing greenhouse gas concentrations and astronomical parameters to their values at 6 ka. Anomalies were calculated for each simulation by subtracting values from preindustrial and mid-Holocene simulations. Implementation of the prescribed vegetation changes varied slightly between these simulations but are consistent with well-established palaeoecological evidence for vegetation changes during the mid-Holocene. In the CESM1.2 simulation, modern-day Sahelian land surface and vegetation at 11° N were prescribed everywhere north of the latitude. In EC-Earth 3.1, Sahara vegetation was prescribed as shrub. In the University of Texas CCSM4 simulation, the Sahara was covered by evergreen shrubs up to 25° N and replaced by a steppe/savanna mix over the rest of North Africa. In GISS-E2.1-G, grass and soil cover was replaced by shrub below 25° N and by grassland over the rest of North Africa. In the simulations with expanded Northern Hemisphere vegetation, areas with modern-day C_3 grass cover were replaced with deciduous forest. Although additional mid-Holocene simulations are now available from the PMIP4[24] experiment, we chose to examine simulations from the PMIP3 experiment for consistency with the generation of models used in the simulations with prescribed vegetation.

The EC-Earth model (pentagons, Fig. 2a,c) shows relatively large warming (0.9 °C) but relatively little additional reduction in winter precipitation associated with prescribed vegetation (1.4%). This appears to be because the model is already exceptionally sensitive to mid-Holocene insolation forcing without vegetation changes, showing warming and winter precipitation declines in simulations forced only with insolation that are comparable to those in other models where prescribed vegetation was included. This finding suggests that the added mid-Holocene warming is responsible for the wintertime precipitation response and implies that wintertime precipitation deficits may be induced by a range of forcings, provided they initiate hemispheric warming.

Sensitivity simulations

Four additional simulations were run to establish how vegetation-mediated changes in surface temperature and sea ice drive changes in atmospheric circulation and rainfall over the North Pacific. These simulations (Supplementary Table 1) were configured using the atmosphere and land components of CESM1.2 forced with regional SST and sea-ice variations derived from the MH and MHveg coupled simulations performed with CESM1.2. All atmosphere–land simulations were run for 200 years with 6 ka insolation and 6 ka greenhouse gas

concentrations and other boundary conditions as described in Supplementary Table 3. The atmospheric circulation response to changes in tropical Pacific SSTs induced by expanded vegetation is quantified by differencing 6kaNorthPacSSTVeg minus 6kaControl. Similarly, the response to North Pacific SSTs is quantified by differencing 6kaNorthPacSSTVeg minus 6kaControl. The 6kaSSTVeg simulation is used to confirm that the wintertime circulation responses over the North Pacific are explained by the combination of the responses to tropical and North Pacific SST changes with a minor role for sea-ice changes (Supplementary Fig. 1).

Ocean heat budget analysis

To analyse the underlying physical mechanisms influencing the prominent characteristics of the North Pacific SST anomaly pattern discussed in this study, we employ a mixed-layer heat budget analysis method following ref. 61. In this analysis, the temperature-forcing contributions from net surface shortwave radiation (Q'_{SW}), net surface longwave radiation (Q'_{LW}), sensible (Q'_{SH}) and latent (Q'_{LH}) heat fluxes, and the heat flux due to ocean dynamics (O') (calculated as a residual) were considered. In addition, contributions from near-surface wind speed ($Q'_{LH,w}$), near-surface relative humidity ($Q'_{LH,RH}$) and air–sea temperature contrasts ($SST'_{LH,\Delta T}$) towards total latent heat flux were considered. The primes denote differences between the perturbed simulation (CESM 6 ka NH + GS_{veg}) and the control simulation (CESM 6 ka PI_{veg}), and overbars denote the climatological mean. As described in ref. 61, the diagnostic equation to show how each forcing term contributes to SST anomalies is as follows:

$$SST' = SST'_{SW} + SST'_{LW} + SST'_{SH} + SST'_{O} + SST'_{LH,w} + SST'_{LH,RH} + SST'_{LH,\Delta T}$$

Where:

$$SST'_{SW} = -\frac{Q'_{SW}}{\alpha \overline{Q_{LH}}} \quad \alpha = \frac{L_v}{R_v T^2} \approx 0.06\,K^{-1}$$

$$SST'_{LW} = -\frac{Q'_{LW}}{\alpha \overline{Q_{LH}}}$$

$$SST'_{SH} = -\frac{Q'_{SH}}{\alpha \overline{Q_{LH}}}$$

$$SST'_{Ocn} = -\frac{O'}{\alpha \overline{Q_{LH}}}$$

$$SST'_{LH,w} = -\frac{Q'_{LH,w}}{\alpha \overline{Q_{LH}}} = -\frac{W'}{\alpha \overline{W}}$$

$$SST'_{LH,RH} = -\frac{Q'_{LH,RH}}{\alpha \overline{Q_{LH}}} = -\frac{RH'_0}{\alpha(e^{\alpha \overline{\Delta T}} - \overline{RH_0})}$$

$$SST'_{LH,\Delta T} = -\frac{Q'_{LH,\Delta T}}{\alpha \overline{Q_{LH}}} = -\frac{\overline{RH_0}\Delta T'}{e^{\alpha \overline{\Delta T}} - \overline{RH_0}}$$

The results of this analysis, the contributions of the two largest components (ocean dynamics and shortwave cloud forcing) to the temperature anomaly are shown in Extended Data Fig. 8.

Proxy–model comparison

To evaluate which climate models most accurately reflect the patterns of SST and hydroclimate changes evident in the proxy data, we followed the approaches devised previously by DiNezio and Tierney[58] and Conroy et al.[62] and computed the weighted Cohen's kappa[58] and Gwet's AC[60] statistics. These approaches categorize the proxy and model data at each location (wet, dry, unchanged or warmer, cooler, unchanged, relative to the preindustrial) and vary the threshold used to determine this categorization to evaluate the robustness of the results (Extended Data Fig. 6 and Supplementary Table 3). The agreement is estimated using the weighted Cohen's k and Gwet's AC statistics, which is the fractional agreement between the proxy and model data at all sites compared with the probability of random agreement. We calculate both statistics as the Gwet's AC is considered to be more robust for skewed datasets[60]. The weighting procedure penalizes sites more when the Holocene–PI change is in the opposite direction between the models and the proxy reconstructions. Because the proxy data are not distributed evenly in space, and to avoid overrepresenting some areas in the model where proxy data density is higher, we applied a 100 km search radius to each site and combined all proxy data reconstructions within that area following DiNezio and Tierney[58].

Data availability

All data produced in our analyses are available in the main text, in the Supplementary Information and via figshare at https://doi.org/10.6084/m9.figshare.28947815 (ref. 52). CESM2 simulations are available for download from http://www.cesm.ucar.edu/experiments/. PMIP3 model output is publicly available from https://pmip3.lsce.ipsl.fr. The additional mid-Holocene simulations investigating vegetation changes using EC-Earth, GISS-E2-G and CCSM4-Toronto, and CESM are available from https://doi.org/10.5281/zenodo.7651155 (ref. 63) and https://zenodo.org/record/6112019#.YhfNZOjMKUm (ref. 64), respectively. All data processing and figures were produced in Python 3.9 using xarray[65], Matplotlib[66] and Cartopy[67].

Code availability

The MixSIAR model is available from https://brianstock.github.io/MixSIAR/. Mixing model code produced during our analysis is available via figshare at https://doi.org/10.6084/m9.figshare.28947815 (ref. 52). Code for model data analysis and figures is available on request.

References

48. Jimenez-Moreno, G., Fawcett, P. J. & Anderson, R. S. Millennial- and centennial-scale vegetation and climate changes during the late Pleistocene and Holocene from northern New Mexico (USA). *Quat. Sci. Rev.* **27**, 1442–1452 (2008).
49. Armour, J., Fawcett, P. J. & Geissman, J. W. 15 ky paleoclimatic and glacial record from northern New Mexico. *Geology* **30**, 723–726 (2002).
50. Blaauw, M. & Christen, J. A. Flexible paleoclimate age–depth models using an autoregressive gamma process. *Bayesian Anal.* **6**, 457–474 (2011).
51. Anderson, R. S., Allen, C. D., Toney, J. L., Jass, R. B. & Bair, A. N. Holocene vegetation and fire regimes in subalpine and mixed conifer forests, southern Rocky Mountains, USA. *Int. J. Wildland Fire* **17**, 96–114 (2008).
52. Todd, V. L. et al. Data and code for 'North Pacific ocean–atmosphere responses to Holocene and future warming drive Southwest US drought'. *figshare* https://doi.org/10.6084/m9.figshare.28947815 (2025).
53. Sachse, D. et al. Molecular paleohydrology: interpreting the hydrogen-isotopic composition of lipid biomarkers from photosynthesizing organisms. *Annu. Rev. Earth Planet. Sci.* **40**, 221–249 (2012).
54. Hou, J. Z., D'Andrea, W. J. & Huang, Y. S. Can sedimentary leaf waxes record D/H ratios of continental precipitation? Field, model, and experimental assessments. *Geochim. Cosmochim. Acta* **72**, 3503–3517 (2008).

55. Stock, B. C. et al. Analyzing mixing systems using a new generation of Bayesian tracer mixing models. *PeerJ* **6**, e5096 (2018).
56. Hersbach, H. et al. The ERA5 global reanalysis. *Q. J. R. Meteorol. Soc.* **146**, 1999–2049 (2020).
57. Herzschuh, U. et al. LegacyClimate 1.0: a dataset of pollen-based climate reconstructions from 2594 Northern Hemisphere sites covering the last 30 kyr and beyond. *Earth Syst. Sci. Data* **15**, 2235–2258 (2023).
58. DiNezio, P. N. & Tierney, J. E. The effect of sea level on glacial Indo-Pacific climate. *Nat. Geosci.* **6**, 485–491 (2013).
59. Cohen, J. Weighted kappa: nominal scale agreement provision for scaled disagreement or partial credit. *Psychol. Bull.* **70**, 213–220 (1968).
60. Gwet, K. L. Testing the difference of correlated agreement coefficients for statistical significance. *Educ. Psychol. Meas.* **76**, 609–637 (2016).
61. Amaya, D. J. et al. Air–sea coupling shapes North American hydroclimate response to ice sheets during the Last Glacial Maximum. *Earth Planet. Sci. Lett.* **578**, 117271 (2022).
62. Conroy, J. L., Karamperidou, C., Grimley, D. A. & Guenthner, W. R. Surface winds across eastern and midcontinental North America during the Last Glacial Maximum: a new data–model assessment. *Quat. Sci. Rev.* **220**, 14–29 (2019).
63. Tiwari, S. On the remote impacts of mid-Holocene Saharan vegetation on South American hydroclimate: a modelling intercomparison. *Zenodo* https://doi.org/10.5281/zenodo.7651155 (2022).
64. Thompson, A. J., Zhu, J., Poulsen, C. J., Tierney, J. E. & Skinner, C. B. Northern Hemisphere vegetation change drives a Holocene thermal maximum. *Zenodo* https://zenodo.org/record/6112019#.YhfNZOjMKUm (2022).
65. Hoyer, S. & Hamman, J. xarray: N–D labeled arrays and datasets in Python. *J. Open Res. Softw.* **5**, 10 (2017).
66. Hunter, J. D. Matplotlib: a 2D graphics environment. *Comput. Sci. Eng.* **9**, 90–95 (2007).
67. Met Office Cartopy: a cartographic Python library with a Matplotlib interface. *Zenodo* https://doi.org/10.5281/zenodo.1182735 (2014).

Acknowledgements

We acknowledge the decades of work by many individual authors who produced the palaeoclimate records used here in the sea surface temperature and hydroclimate data syntheses. We also acknowledge the organizers and all the modellers who contributed mid-Holocene simulations to the Paleoclimate Modeling Intercomparison Project, Phase 3 (PMIP3). The CESM project is supported primarily by the National Science Foundation (NSF). This material is based on work supported by the National Center for Atmospheric Research (NCAR), a major facility sponsored by the NSF under Cooperative Agreement no. 1852977. The CAM6 Prescribed SST GOGA experiments were conducted by the Climate Variability and Change Working Group (CVCWG). Record generation, data synthesis, model comparisons and sensitivity simulations were funded by the US National Science Foundation P2C2 programme awards 1702271 to T.M.S. and 2002528 to T.M.S. and P.N.D. F.S.R.P. acknowledges financial support from the NSERC Discovery Grant (grant RGPIN-2018-04981) and the NOVA—FRQNT-NSERC (grants 2023-NOVA-324826 and ALLRP 577112-22).

Author contributions

T.M.S. and P.N.D. conceived the study. The records were generated by T.M.S. and V.L.T. T.M.S., P.N.D. and V.L.T. developed the methodology. The investigation was conducted by T.M.S., P.N.D., V.L.T. and J.M.K. Samples were collected by R.S.A., P.J.F. and G.J.-M. Climate simulations were provided by F.S.R.P., A.N.L., A.J.T. and J.Z. V.L.T., T.M.S. and P.N.D. wrote the paper. All authors reviewed and edited the final version of the paper.

Competing interests

The authors declare no competing interests.

Additional information

Extended data is available for this paper at https://doi.org/10.1038/s41561-025-01726-z.

Supplementary information The online version contains supplementary material available at https://doi.org/10.1038/s41561-025-01726-z.

Correspondence and requests for materials should be addressed to Victoria L. Todd.

Peer review information *Nature Geoscience* thanks Dimitris Herrera and the other, anonymous, reviewer(s) for their contribution to the peer review of this work. Primary Handling Editor: James Super, in collaboration with the *Nature Geoscience* team.

https://doi.org/10.1038/s41561-025-01726-z

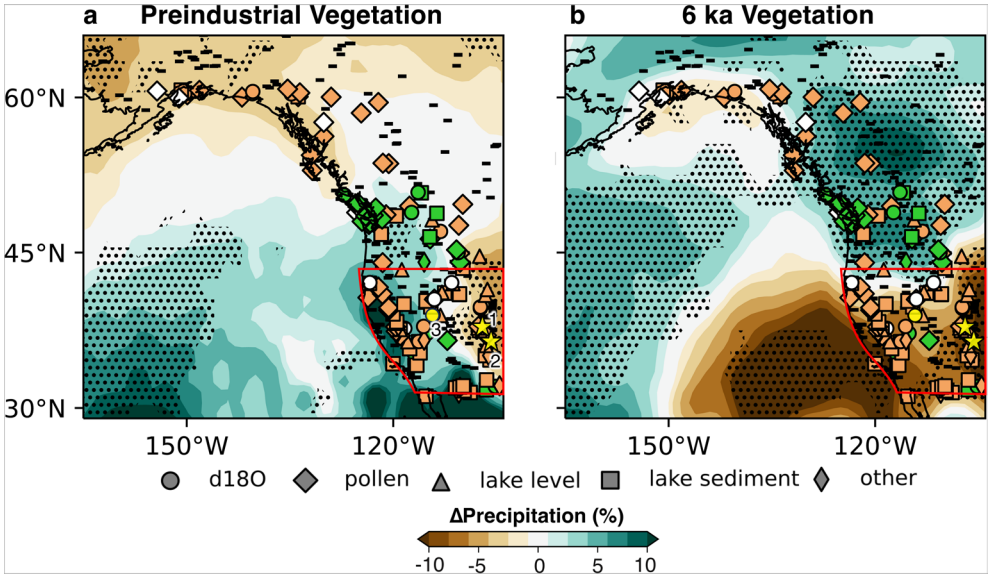

Extended Data Fig. 1 | Proxy and Model Precipitation Changes in the Mid-Holocene. Locations of sites from this study (stars: 1- Hunters Lake, 2- Stewart Bog) and synthesized proxy hydroclimate data (symbols) compared against simulated winter (DJF) precipitation (shading) from the ensemble of mid-Holocene experiments with (**a**) preindustrial vegetation (from PMIP3) and with (**b**) prescribed 6 ka vegetation (this study). Symbols indicate the proxy type: $\delta^{18}O$ (circles), pollen transfer functions (diamonds), lake level (triangles), lake sediment (squares), and others (thin diamonds). The isotope record from 3-Leviathan Cave is indicated with a yellow circle. Stippling indicates where the majority of models agree (**a**: 8/15; **b**: 5/8). The red box indicates the area used to calculate changes in precipitation in the Southwest US, which is the same as in ref. 8.

https://doi.org/10.1038/s41561-025-01726-z

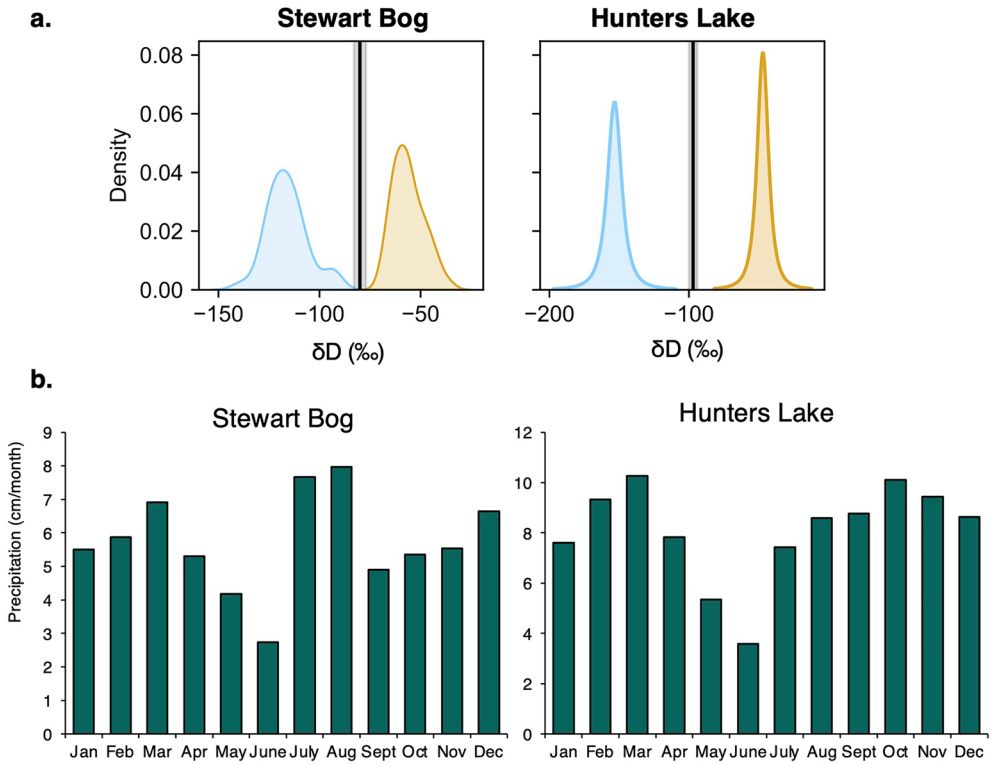

Extended Data Fig. 2 | Seasonal δD Distribution and Modern Precipitation at Study Sites. (**a**) Probability density plots of the seasonal distribution of modern precipitation δD for Stewart Bog, NM[20] and Hunters Lake, CO[23] from the Online Isotopes in Precipitation Calculator (OIPC)[23] Winter (DJF) and summer (JAS) values are shown in blue and gold, respectively. The solid black line with grey shading indicates the annual average and 95% CI for each site. (**b**) Monthly averaged precipitation (cm/month) between 1980 and 2019 ref. 28 for Stewart Bog and Hunters Lake.

https://doi.org/10.1038/s41561-025-01726-z

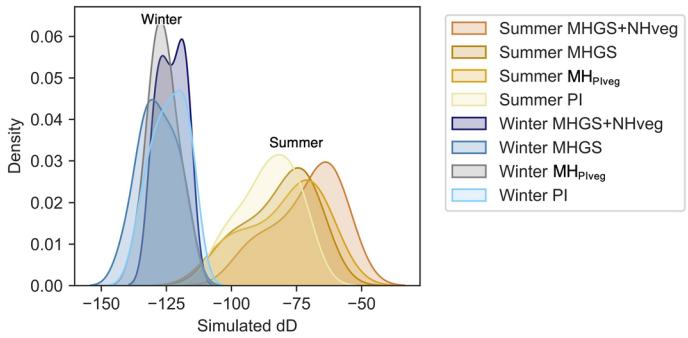

Extended Data Fig. 3 | Simulated Seasonal δD Values Across Holocene Forcing Scenarios. Probability density plots of simulated δD seasonal precipitation for winter (DJF, blue-grey) and summer (JAS, orange-yellow) over the region including our two study locations (−107°W, −105°W, 35°N, 38°N) from i-CESM1.2. PDFs are shown for simulations with boundary conditions and forcings for: preindustrial (PI), mid-Holocene with preindustrial vegetation (MH$_{PIveg}$), mid-Holocene with prescribed "Green Sahara" (GS), mid-Holocene with prescribed "Green Sahara" and high latitude vegetation (MHGS+NH$_{veg}$)[25].

https://doi.org/10.1038/s41561-025-01726-z

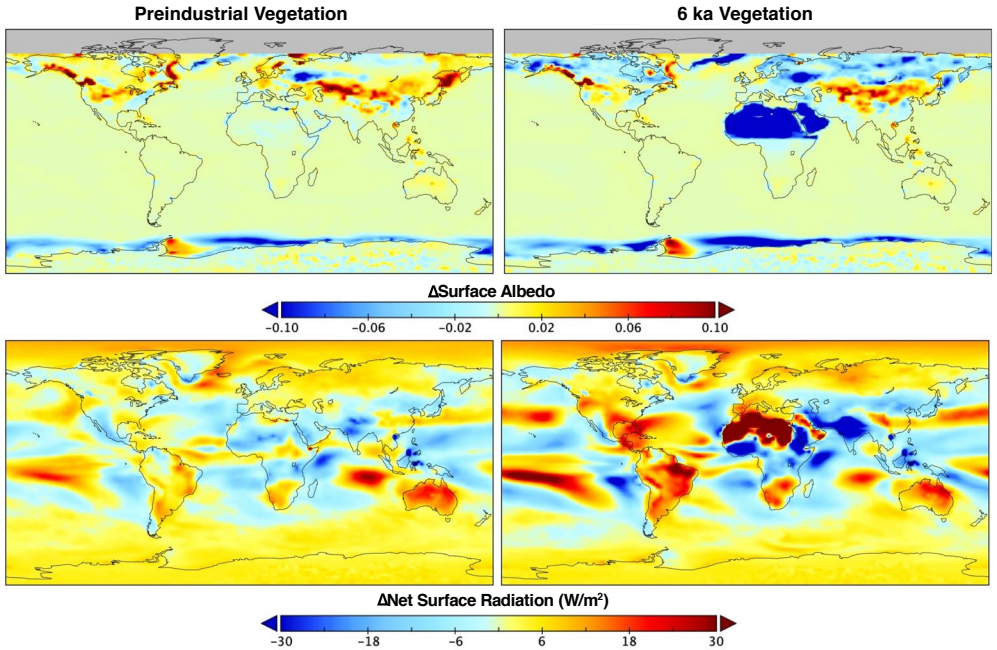

Extended Data Fig. 4 | Impact of Vegetation on Albedo and Surface Radiation. Surface albedo and net surface radiation (W/m^2) anomalies (6 ka-preindustrial) for the CESM1 simulation forced by preindustrial vegetation and insolation only (left) and 6ka conditions with prescribed "Green Sahara" and Northern Hemisphere vegetation changes (right), from ref. 25. Compared with the simulation with insolation only (left), the prescribed vegetation simulation shows an increase in surface radiation localized over regions with expanded vegetation due to the associated reductions in surface albedo (right).

https://doi.org/10.1038/s41561-025-01726-z

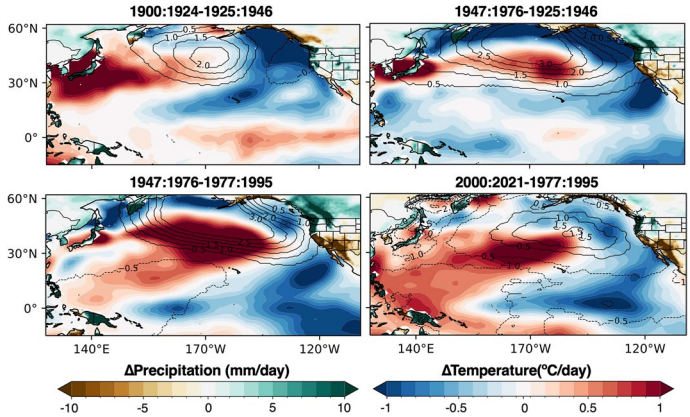

Extended Data Fig. 5 | PDO Epoch Differences in North Pacific Hydroclimate. Differences in winter precipitation over land (shading)[28], sea surface temperature (shading)[46], and sea level pressure (hPa 10 yr^{-1}; contours)[45] trends between epochs with negative (1900:1924, 1947:1995, and 2000:2021) and positive (1925:1946 and 1977:1995) values of the Pacific Decadal Oscillation (PDO) index (data from ref. 33).

https://doi.org/10.1038/s41561-025-01726-z

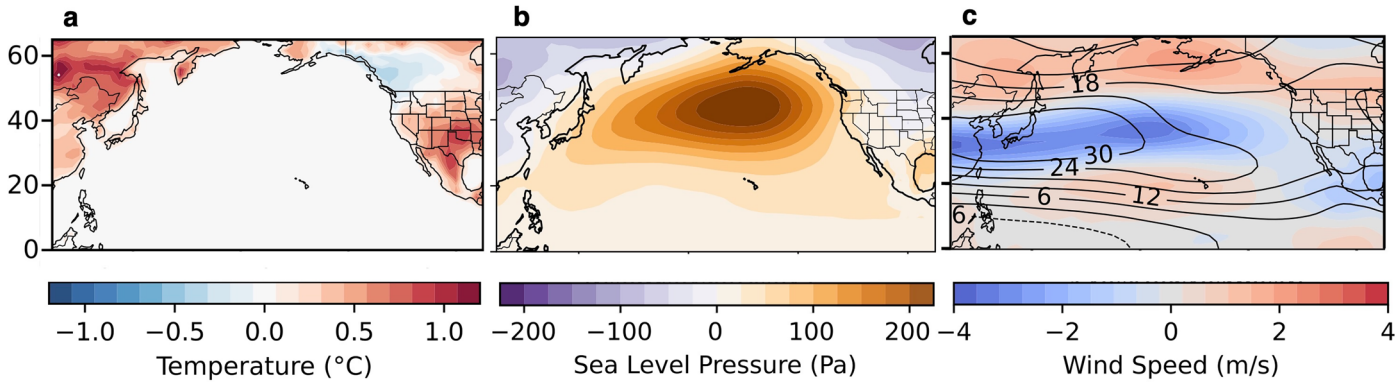

Extended Data Fig. 6 | Vegetation-Driven Changes in the Aleutian Low and Jet Stream. The role of prescribed vegetation (6kaVegetation – 6kaControl) in driving the weakening of the Aleutian Low and the northward shift of the Pacific jet stream in sensitivity experiments with prescribed 6ka Control SSTs (Methods). Annual mean anomalies in **a**. surface temperature, **b**. sea level pressure, and **c**. zonal wind speed (m/s) at 200 hPa (shading), with control-run contours (black lines) overlaid. **b**. Shows the weakening of the Aleutian Low and **c**. the northward shift of the North Pacific jet stream resulting from vegetation-driven **a**. land surface warming.

https://doi.org/10.1038/s41561-025-01726-z

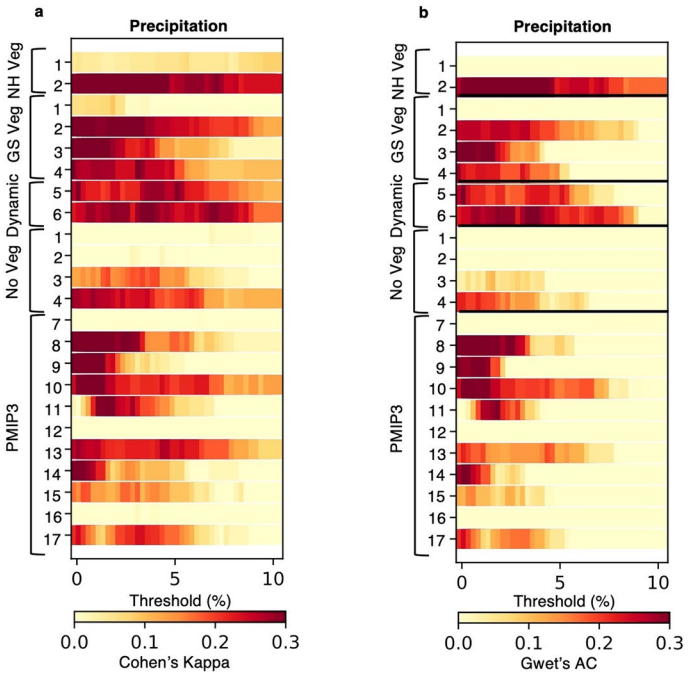

Extended Data Fig. 7 | Model Agreement Metrics for Mid-Holocene Precipitation Change. a. Cohen's κ and **b**. Gwet's AC for the models as a function of wetter/drier thresholds. Greater agreement is evident in the majority of the models with dynamic or prescribed vegetation. The numbers refer to the following models: 1-GISS-E2-G, 2-CESM1.2, 3-Toronto-CCSM4, 4-EC-Earth, 5-HadGEM2-ES, 6-HadGEM2-CC, 7-CCSM4,8-MPI-ESM-P, 9-IPSL, 10-CSIRO-Mk3, 11-Fgoals-g2, 12-bcc-csm-1, 13-CGCM3, 14-CNRM-CM5, 15-MIROC-ESM, 16-GISS-E2-R, 17-Fgoals-s2.

https://doi.org/10.1038/s41561-025-01726-z

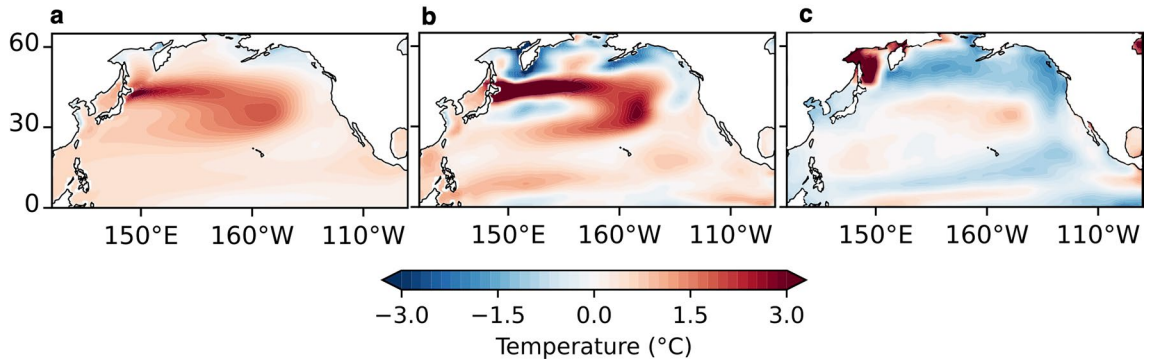

Extended Data Fig. 8 | Ocean Feedbacks Driving North Pacific SST Patterns. The role of **b**. Ocean Dynamical Adjustments and **c**. Shortwave cloud forcing in driving the **a**. sea surface warming temperature pattern in the North Pacific in the fully coupled CESM1 mid-Holocene simulation with prescribed 'Green Sahara' and Siberian vegetation changes ref. 25. Results from Heat Budget Analysis following ref. 61.

https://doi.org/10.1038/s41561-025-01726-z

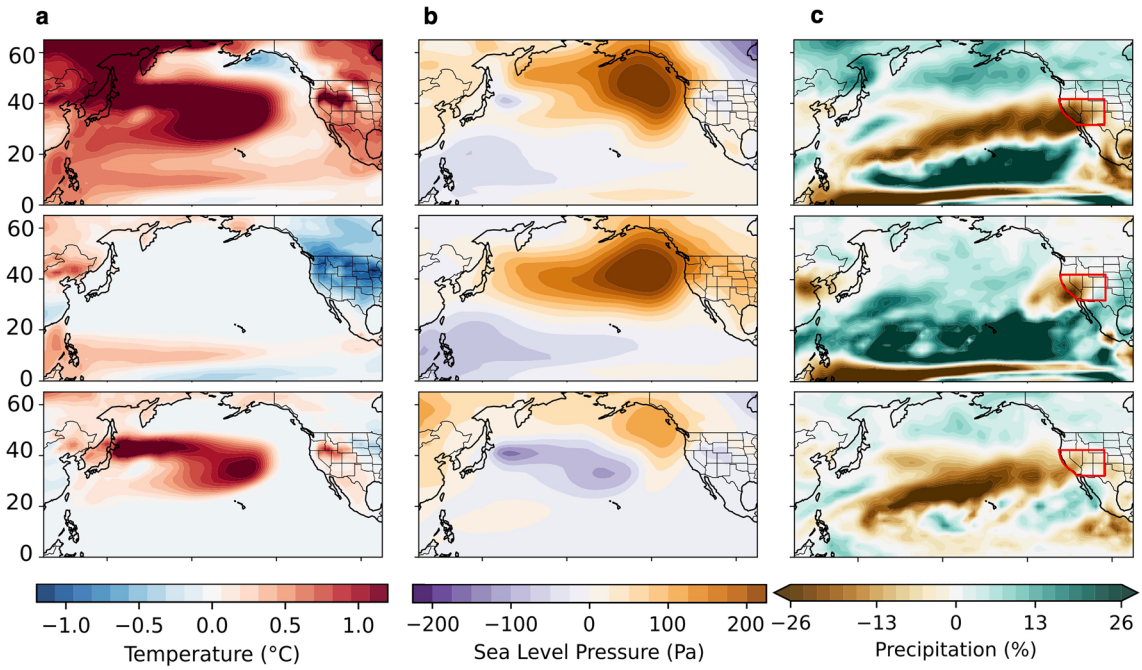

Extended Data Fig. 9 | Sensitivity to SST Boundary Conditions in Driving Mid-Holocene Climate. Sensitivity experiments (Methods, Supplementary Table 3) illustrating winter (DJF) anomalies in **a**) surface temperature (ΔT, °C), (**b**) sea level pressure (Pa), and (**c**) large-scale precipitation (ΔP, %) relative to a 6 ka control run (6kaControl). Each row shows results with different prescribed SST boundary conditions taken from the coupled vegetation experiment[25]: Global SSTs and sea ice (6kaSSTVeg) (top row), Only Tropical Pacific SSTs (6kaTropPacSSTVeg) (middle row), and Only North Pacific SSTs (6kaNorthPacSSTVeg) (bottom row). These distinctions highlight the critical role of extratropical ocean forcing in shaping the mid-Holocene winter climate, beyond the tropical influences alone. Red boxes indicate the area used to calculate Southwest US drought anomalies.

https://doi.org/10.1038/s41561-025-01726-z

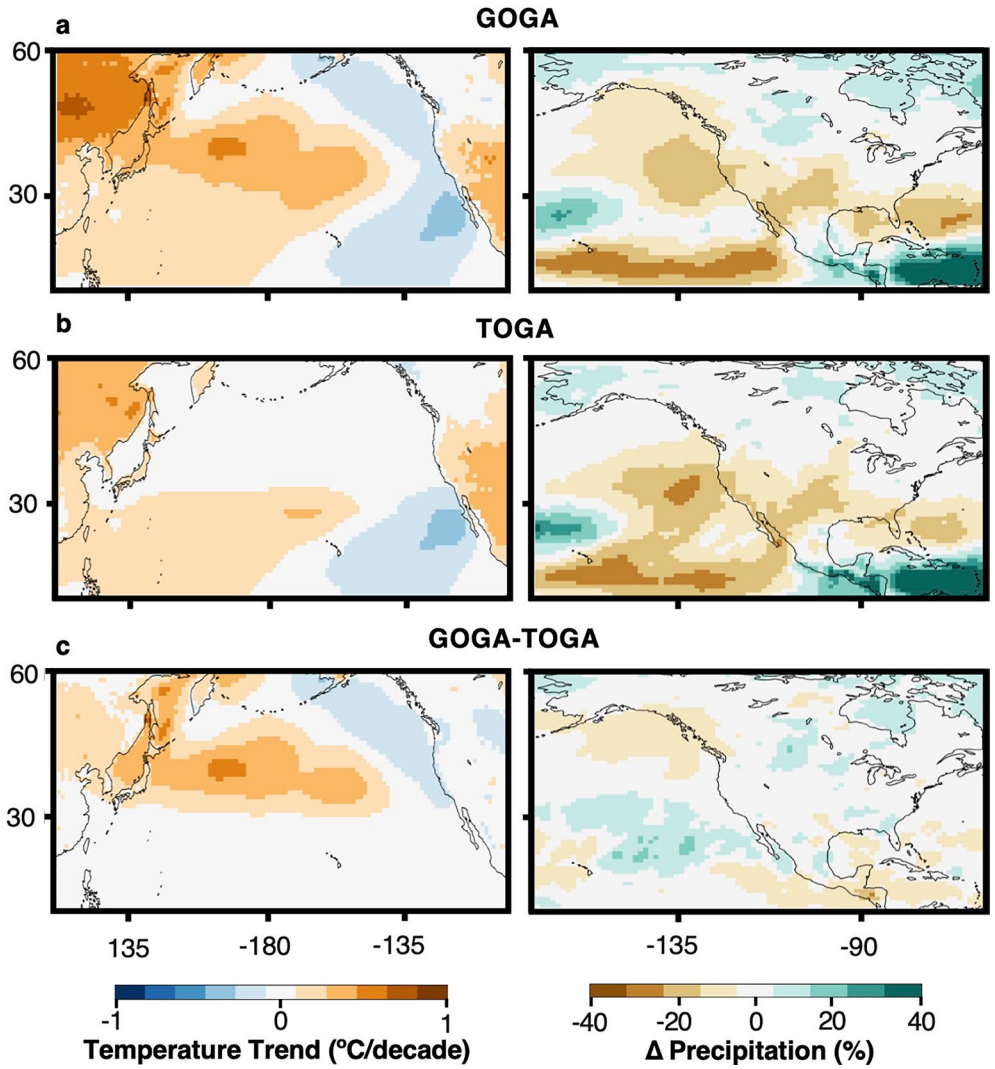

Extended Data Fig. 10 | Observed-Model Comparison of Ocean Forcing on North American Climate. Temperature trends (°C/decade) and precipitation changes (%) from 1983 to 2019 in the simulations from the **a**) Global Ocean Global Atmosphere (GOGA) and **b**) Tropical Ocean Global Atmosphere (TOGA) simulations as in ref. 8. **c**) The difference between the GOGA and TOGA experiments. The GOGA and TOGA simulations were completed by the NCAR Climate Variability and Change Working Group. This data is available from the NCAR Climate Data Gateway.